

PAPER • OPEN ACCESS

## Protocols for x-ray transient grating pump/optical probe experiments at x-ray free electron lasers

To cite this article: Danny Fainozzi *et al* 2024 *J. Phys. B: At. Mol. Opt. Phys.* **57** 185403

View the [article online](#) for updates and enhancements.

You may also like

- [Low frequency coherent Raman spectroscopy](#)  
Randy A Bartels, Dan Oron and Hervé Rigneault
- [Convolutional neural network for transient grating frequency-resolved optical gating trace retrieval and its algorithm optimization](#)  
Siyuan Xu, , Xiaoxian Zhu et al.
- [Transient grating study of the intermolecular dynamics of liquid nitrobenzene](#)  
Hong-Lin Wu, , Yun-Fei Song et al.

# Protocols for x-ray transient grating pump/optical probe experiments at x-ray free electron lasers

Danny Fainozzi<sup>1,\*</sup> , Riccardo Cucini<sup>2</sup>, Joan Vila-Comamala<sup>3</sup>, Frederico Lima<sup>4</sup>, Fernando Ardana-Lamas<sup>4</sup>, Luis Bañares<sup>5,6</sup>, Matias Bargheer<sup>7</sup>, Filippo Bencivenga<sup>8</sup> , Nadia Berndt<sup>9</sup> , Martin Beye<sup>10,11</sup> , Mykola Biednov<sup>4</sup>, Stefano Bonetti<sup>12</sup> , Marta Brioschi<sup>2,13</sup>, Andrea Cannizzo<sup>1</sup>, Pietro Carrara<sup>2,13</sup> , Majed Chergui<sup>14</sup> , Christian David<sup>3</sup> , Robin Y Engel<sup>11</sup> , Eugenio Ferrari<sup>11</sup> , Thomas Feuer<sup>1,4</sup>, Paul Frankenberger<sup>4</sup>, Wojciech M Gawelda<sup>5,15</sup>, Alessandro Gessini<sup>8</sup>, Siti Heder<sup>4</sup>, Xinchao Huang<sup>4</sup> , Nupur N Khatu<sup>4,8,12</sup>, Martin Knoll<sup>4</sup>, Anders Madsen<sup>4</sup>, Talgat Mamyrbayev<sup>3</sup>, Claudio Masciovecchio<sup>8</sup>, Alexei A Maznev<sup>9</sup>, Christopher Milne<sup>4</sup> , Riccardo Mincigrucci<sup>8</sup>, Keith A Nelson<sup>9</sup>, Ettore Paltanin<sup>8,16</sup>, Giorgio Rossi<sup>2,13</sup>, Markus Scholz<sup>11</sup>, Carles Serrat<sup>17</sup> , Urs Staub<sup>3</sup>, Jakub Szlachetko<sup>18</sup>, Renato Torre<sup>19,20</sup> , Mano R Dhanalakshmi-Veeraraj<sup>3</sup>, Han Xu<sup>4</sup>, Peter Zalden<sup>4</sup> and Cristian Svetina<sup>4,5,\*</sup>

<sup>1</sup> Institute of Applied Physics, University of Bern, Sidlerstrasse 5, 3012 Bern, Switzerland

<sup>2</sup> CNR-IOM, SS 14 km 163.5 in AREA Science Park, 34149 Trieste, Italy

<sup>3</sup> Paul Scherrer Institute PSI, Forschungsstrasse 111, 5232 Villigen, Switzerland

<sup>4</sup> European x-ray Free-Electron Laser Facility, Holzkoppel 4, 22869 Schenefeld, Germany

<sup>5</sup> IMDEA Nanociencia, C. Faraday 9, 28049 Madrid, Spain

<sup>6</sup> Departamento de Química Física and Center for Ultrafast Lasers, Facultad de Ciencias Químicas, Universidad Complutense de Madrid, 28040 Madrid, Spain

<sup>7</sup> Institut für Physik und Astronomie, Karl-Liebknecht-Strasse 24-25, 14476 Potsdam, Germany

<sup>8</sup> Elettra Sincrotrone Trieste, SS 14 km 163.5 in AREA Science Park, 34149 Trieste, Italy

<sup>9</sup> Massachusetts Institute of Technology MIT, 77 Massachusetts Avenue, Cambridge, MA 02139, United States of America

<sup>10</sup> Department of Physics, Stockholm University, Stockholm, Sweden

<sup>11</sup> Deutsches Elektronen-Synchrotron DESY, Notkestraße 85, 22607 Hamburg, Germany

<sup>12</sup> Department of Molecular Sciences and Nanosystems, Ca' Foscari University of Venice, Venice, Italy

<sup>13</sup> Dipartimento di Fisica, Università degli Studi di Milano, via G. Celoria 16, 20133 Milano, Italy

<sup>14</sup> Ecole Polytechnique Fédérale de Lausanne EPFL, Lausanne Centre for Ultrafast Science LACUS, ISIC, 1015 Lausanne, Switzerland

<sup>15</sup> Departamento de Química, Universidad Autónoma de Madrid, Ciudad Universitaria de Cantoblanco, 28049 Madrid, Spain

<sup>16</sup> Department of Physics, Università degli Studi di Trieste, 34127 Trieste, Italy

<sup>17</sup> Department of Physics, Polytechnic University of Catalonia, Colom 11, 08222 Terrassa, Barcelona, Spain

\* Authors to whom any correspondence should be addressed.



Original Content from this work may be used under the terms of the [Creative Commons Attribution 4.0 licence](https://creativecommons.org/licenses/by/4.0/). Any further distribution of this work must maintain attribution to the author(s) and the title of the work, journal citation and DOI.

<sup>18</sup> SOLARIS National Synchrotron Radiation Centre, Jagiellonian University, Krakow, Poland

<sup>19</sup> European Laboratory for Non-linear Spectroscopy LENS and Dip. di Fisica ed Astronomia, University of Firenze, Via N. Carrara, 1, 50019 Sesto Fiorentino, Italy

<sup>20</sup> Istituto Nazionale di Ottica, INO-CNR, L.go E. Fermi 6, 50125 Firenze, Italy

E-mail: [danny.fainozzi@unibe.ch](mailto:danny.fainozzi@unibe.ch) and [cristian.svetina@imdea.org](mailto:cristian.svetina@imdea.org)

Received 12 January 2024, revised 1 August 2024

Accepted for publication 20 August 2024

Published 29 August 2024



## Abstract

Transient grating spectroscopy is a specialized application of the four-wave-mixing methodology and constitutes a versatile technique for investigating the dynamics of vibrational, magnetic and electronic degrees of freedom of matter in a background-free fashion. Recent developments in free-electron laser sources have enabled the extension of this technique into the extreme ultraviolet range. Ongoing efforts to expand transient grating spectroscopy into the x-ray regime promise numerous advantages: (1) substantial penetration depths that allow for probing bulk material properties, (2) element specificity via specific core-excited states, and (3) short wavelengths that allow for excitation gratings with higher momentum transfer and improved spatial resolution. In this study, we comprehensively outline the procedures for conducting x-ray transient grating pump/optical probe experiment. The process encompasses the design and alignment of the experimental setup, as well as the subsequent steps involved in data acquisition and analysis. This paper is intended as a comprehensive guide for researchers interested in implementing x-ray transient grating spectroscopy, providing valuable insights into the intricacies of the experimental workflow required for this novel technique. Furthermore, we discuss the potential for extending this methodology to an x-ray pump/x-ray probe scheme, envisioning a future direction that holds promise for enhancing the capabilities and scope of x-ray transient grating spectroscopy, opening new opportunities for studying ultrafast processes with unprecedented temporal and spatial resolutions.

Keywords: free electron laser, ultrafast, x-ray, transient grating

## 1. Introduction

The constant pursuit of discovering novel materials with unparalleled behaviour relies on specialized techniques capable of measuring their properties with unprecedented spatial-temporal and/or energy resolutions. Amid various methodologies, those adept at selectively defining the length scale of acquired signals are garnering increased attention. Their proficiency in comprehending length-scale dependencies plays a pivotal role in understanding the physics and propelling technology toward nanometre scales where many physical properties show a transitional behaviour, such as ballistic to diffusive electron and phonon transport, occur [1, 2]. These length-scales are uniquely accessible through wave-mixing techniques, as they fall in between the ranges of other techniques such as Brillouin scattering, Raman spectroscopy (smaller  $q$ -range), inelastic neutron scattering or inelastic x-ray scattering (less  $q$  resolution) or techniques that intrinsically modify the sample under investigation.

An approach to investigate various length scales involves the degenerate form of four-wave mixing, referred to as transient grating (TG). Typically, TG utilizes two identical

intersecting pump beams that are spatially and temporally overlapped on the sample, thereby generating the excitation transient grating through interference. Subsequently, a time-delayed third pulse i.e. the probe, is diffracted by the excited material in accordance with a momentum-conservation law known as the phase-matching condition, generating a background-free signal. Assuming the sample is orthogonal to the bisector of the pump beams, the period  $\Lambda_{\text{TG}}$  of the transient grating on the sample is determined by the crossing angle  $2\theta$  and the wavelength  $\lambda$  of the pump beams, following the relation:

$$\Lambda_{\text{TG}} = \frac{\lambda}{2 \sin \theta}. \quad (1)$$

The extension of the TG technique to the extreme ultraviolet (EUV) range has been first realized through the TIMER endstation [3, 4] at the FERMI free electron laser (FEL). TIMER employs the same principle of splitting and recombining single laser pulses on the sample, enabling the generation of gratings with periodicities ranging from 120 to 16 nm [5], with the potential to achieve a single-digit nanometre scale [3].

This capability presents numerous opportunities, including the examination of transport processes at tens of nanometre scales, and being resonant to specific element edges, such as the M-edges of 3d transition metals. However, the EUV wavelengths still impose limitations on the ultimate spatial resolution of the TG method and its ability to directly probe the bulk of the material. An extension to the hard x-ray regime would enable the attainment of sub-nanometre spatial resolutions in the bulk, offering element selectivity for most elements present in condensed matter systems.

In this study, we consolidate insights acquired from experiments conducted as part of a long-term proposal at the European x-ray free electron laser (EuXFEL). We introduce a protocol that enables the user community to conduct x-ray TG pump/optical probe experiments at x-ray FELs (XFELs), capitalizing on the high repetition rate, when accessible.

## 2. Generation of the transient grating

As we move towards shorter wavelengths, employing the traditional splitting and recombination method for generating the transient grating becomes increasingly challenging. Consequently, our initial approach to creating an interference pattern on the sample diverged from the conventional split and recombination methodology used in optical and EUV TG. Instead, we opted for leveraging the Talbot effect, a phenomenon extensively detailed elsewhere [6–8]. The Talbot effect, a natural outcome of Fresnel diffraction, exploits the interaction between a (x-ray) laser beam and a physical mask (grating, whether amplitude or phase) to generate a self-replica of the grating at the sample position, constituting an intensity grating (figure 1). This interference pattern manifests at specific positions along the beam propagation, referred to as ‘Talbot planes’, which collectively form the Talbot carpet. The effect results from the interference of diffraction orders generated by the physical grating. The maximum distance covered by the grating’s image corresponds to the overlapping distance of the  $\pm 1$  diffraction orders, as illustrated in figure 1(a), limited by the beam or grating size. As the sample is moved farther away from the mask, the transient grating produced contains fewer grating lines (i.e. a smaller overlapping region between the orders), leading to a decrease in fringe visibility.

In figure 1(b), a simulation of the Talbot carpet is presented for an x-ray beam at 7.1 keV. This interference pattern exhibits two distinct periodicities: in the  $x$ -direction, which is transverse to the propagation direction, it replicates the period of the physical (i.e. *solid*) grating (representative of our TG). Importantly, this period remains independent of the wavelength used for its generation. In the propagation direction, the pattern reveals the formation of Talbot planes, periodically positioned at a distance of

$$Z_T(m) = m \cdot \frac{2a^2}{\lambda} \quad (2)$$

where  $m \in \mathbb{N}$  represents the index of Talbot planes, and  $a$  is the period of the grating [9, 10]. However, it is crucial to note

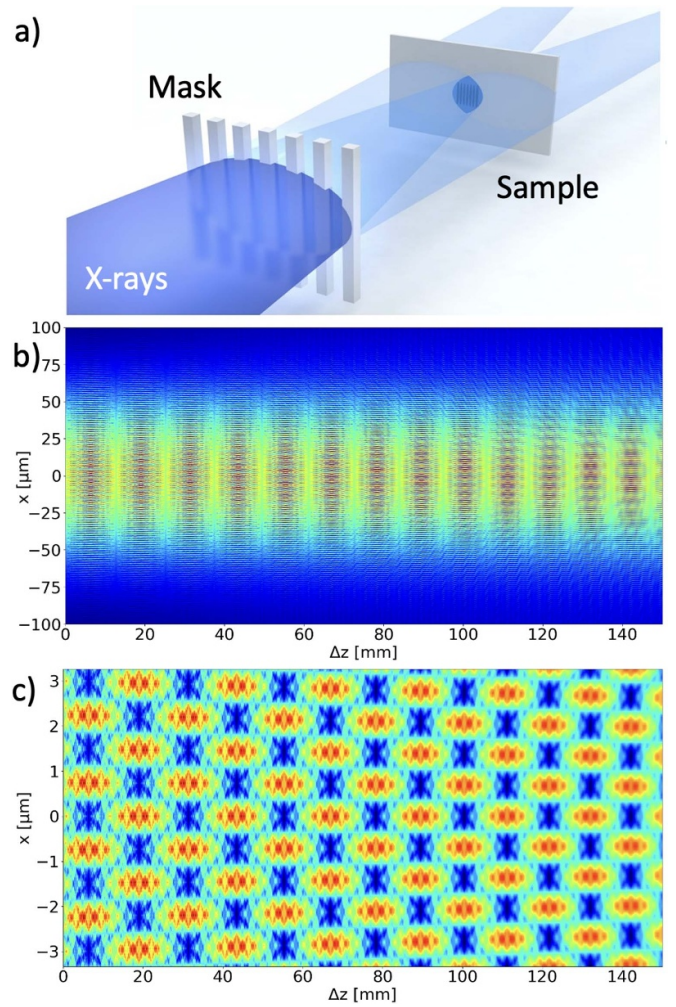


**Figure 1.** Panel (a) depicts a single x-ray beam interacting with a physical grating resulting in the generation of multiple diffraction orders. The interference of these orders produces the Talbot Carpet, faithfully replicating the image of the physical grating downstream. In panel (b), a simulation of the Talbot Carpet is presented, achieved through the Fresnel propagation of a 7.1 keV (0.1% bandwidth) convergent Gaussian beam (100  $\mu\text{m}$  full width at half-maximum (FWHM)) interacting with a 1.5  $\mu\text{m}$   $\pi/2$  phase grating. The  $x$  direction is parallel to the physical grating,  $\Delta z$  is the distance between the physical grating and the sample position. Panel (c) offers a close-up view of the simulated Talbot Carpet presented in panel (b).

that as  $m$  increases, the Talbot image generated at  $Z_T$  gradually deviates from the original mask. This is evidenced by the emergence of weak high spatial frequency structures on top of the TG, as detailed in [11]. While these findings were based on the interaction of a plane wave with a physical grating, slight variations occur when considering a more realistic Gaussian beam. Using a convergent (divergent) Gaussian beam results in a proportional decrease (increase) in the period of its image, determined by the curvature radius of the beam. This alteration also affects the distances between Talbot planes [7, 12] (see figures 1(b) and (c) [13]). Nevertheless, our practical experience indicates that, in most cases, employing a spherical wave approximation is sufficient [14].

It is worth noting that utilizing a phase grating allows the generation of an image with a period similar to that of the original grating ( $\pi/2$  phase) or half of the original grating's period ( $\pi$  phase), achieved by suppressing the transmitted beam in the latter case. However, a significant limitation lies in the manufacturing of the physical grating, which, even with state-of-the-art methods, is typically limited to tens of nanometres due to the challenging aspect ratio between groove height and grating period required for x-ray-gratings.

### 3. TG method and experimental setup

The Transient Grating (TG) technique delves into the third-order nonlinear responses of a sample under investigation. The resulting signal encapsulates these nonlinearities in the form of a third-rank tensor, denoted as  $\chi^{(3)}$ . This tensor is multiplied by the intensities of both pump beams ( $I_{x\text{-rays}}$ ) and the probe beam ( $I_{\text{Laser}}$ ), and further scaled by a factor that accounts for the phase-matching condition ( $\Delta k$ ) [3], following the relation:

$$I_{\text{TG}} \propto \left| \chi^{(3)} I_{x\text{-rays}} I_{\text{Laser}}^{1/2} \frac{L}{\lambda_{\text{pr}}} \text{sinc} \left( \frac{\Delta k L}{2} \right) \right|^2. \quad (3)$$

Here,  $\lambda_{\text{pr}}$  represents the wavelength of the probe beam,  $L$  denotes the interaction length within the sample, and  $\Delta k$  is the projection along the sample normal of the wavevector difference between the incoming (probe) and outgoing (signal) photons. The signal is maximized when  $\Delta k = 0$  i.e. when the Bragg condition is satisfied in such a way that the incidence angle of the probe beam equals its diffracted angle. As depicted in figure 2, employing a large phase mask period along with the optical laser probe relaxes the phase-matching condition, allowing for a few % misalignment in the incident angle, resulting in a modest reduction in signal intensity. However, this constraint becomes more stringent as the period of the grating decreases and the wavelengths of the probe beam become shorter.

Equation (3) highlights the necessity for the setup to be meticulously designed to ensure the fulfilment of the phase-matching condition. Simultaneously, any setup should facilitate the accurate measurement of both x-ray ( $I_{x\text{-rays}}$ ) and laser ( $I_{\text{Laser}}$ ) intensities to serve as normalization factors, accounting for the intensity fluctuations in the beams.

#### 3.1. The laser pre-alignment

The operational beamtimes granted by FELs are characterized by short and intense workflows and need to be managed efficiently. To optimize the outcomes within the allocated time, thorough preparation is essential. In our case, we have developed a method to align the optical laser and detection setup ahead of the beamtime, in the absence of x-rays.

To pre-align the setup, a grating with a period equal to the expected TG period is positioned at the sample location. The laser, entering from the right, strikes a mirror set at  $45^\circ$  and

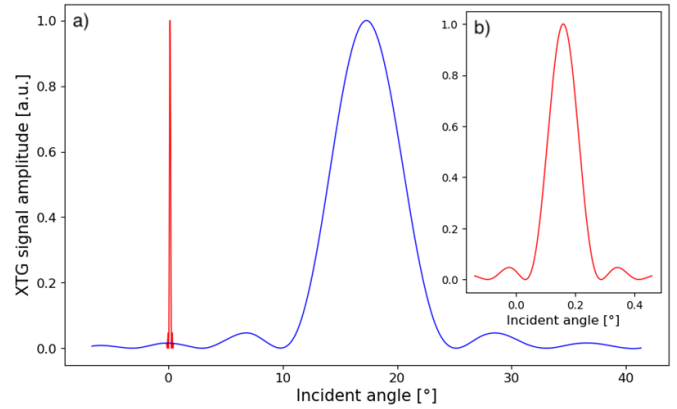


**Figure 2.** Shows simulations of the  $|\text{sinc}(\Delta k L / 2)|^2$  part of equation (3). (a) A comparison of phase-matching conditions is presented for two cases, assuming the interaction length  $L$  as the absorption length of silicon for the respective wavelengths. The blue curve corresponds to a 7.1 keV pump, 800 nm probe, and a  $1.5 \mu\text{m}$   $\pi/2$  phase grating, generating a  $1.34 \mu\text{m}$  TG due to the Gaussian beam convergence. In red is the case of a 7.1 keV pump, 9.9 keV probe, and a  $50 \text{ nm}$   $\pi$  phase mask, resulting in a  $22 \text{ nm}$  TG at the sample. The higher energy of the probe, coupled with the smaller period of the phase grating, necessitates a more precise fulfilment of the phase-matching angle. As visible in the zoom-in (b), the FWHM is approximately  $0.1^\circ$  compared to the approximately  $7^\circ$  of the more relaxed case.

passes through a beam splitter, which directs a small portion of the beam to a photodiode (placed on a translation stage) for use as the normalization factor  $I_{\text{Laser}}$  in equation (3) (see figure 3). The beam advances to the second mirror (on a rotation stage) and is reflected toward the mask, which will subsequently generate the transient grating. A photodiode on a translational stage is positioned to observe the laser beam transmitted through the sample, while an array of detectors (also on a translation stage) is placed in the forward diffraction position to capture the TG signal. The rotational angle and position of the D-mirror are adjusted based on the expected phase-matching angle for the mask's period, ensuring the fulfilment of the phase-matching condition and maximizing the TG signal. The detector position can be fine-tuned by directing the laser onto the grating and centring its position on the diffracted beam. Alternatively, the mask can be removed, and a thin transparent glass placed at the sample position, with a mirror in the transmission direction and orthogonal to it, as depicted in figure 3(b). The mirror back-reflects the light onto the glass, which in turn reflects part of it towards the direction of the XTG signal. In this latter case, the detection of the XTG signal in back-diffraction can be configured using the same mirror. Part of the back-reflected light by the mirror passes through the thin glass sample, returning to the D-shaped mirror, where it is deflected by the beam splitter to a photodiode. It is essential to note that to maximize the signal, the laser beam at the sample position should have vertical and horizontal dimensions similar with respect to the x-ray beam.

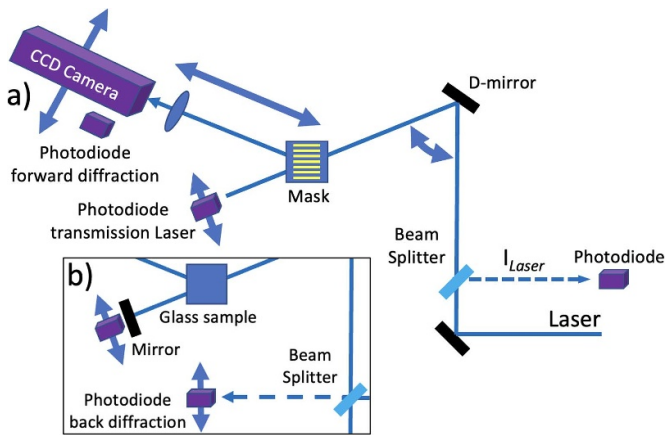


**Figure 3.** A schematic of the XTG setup implemented at the FXE Instrument at the European XFEL is depicted in (a). The laser, entering from the right, is reflected by a mirror and guided through a beam splitter. A portion of the signal (the percentage determined by the intensity of the XTG signal) is redirected to the right and captured by a photodiode for use as a normalization factor ( $I_{\text{Laser}}$ ). The remaining beam proceeds to the second mirror, whose angle can be adjusted to satisfy the phase-matching condition dictated by the TG period at the sample position. A photodiode is positioned on the trajectory of the transmitted beam, while a set of detectors, consisting of a photodiode and a CCD camera in this case, are located at the position of the forward-diffracted signal. A collimating lens is placed before the detection point. Alternatively, instead of using the phase mask, a thin glass sample can be placed at the sample position while a mirror is positioned in the transmission direction, orthogonal to it, as illustrated in insert (b). If the sample of interest is opaque, or if the user desires to collect both forward- and back-diffraction signals simultaneously, back-diffraction detection can be tested using the mirror that back-reflects the transmitted beam. A portion of the signal is directed back to the D-shaped mirror, deflected by the beam splitter, and directed to a photodiode.

Measuring the signal in forward diffraction mode using this hybrid x-ray pump/optical probe technique is affected by walk-off or smearing due to the differences in the refractive indices, and, consequently, velocities, between x-rays and optical light. In a first approximation, this is a constant contribution during a single measurement. However, it may vary when changing wavelengths, requiring careful consideration during comparisons. One possible solution to estimate the smearing effect is to simultaneously measure the signal in both forward and backward diffraction modes.

### 3.2. Alignment with x-rays

The initial stages of x-ray measurements entail a few modifications to the setup compared to the pre-alignment. A test sample is placed at the nominal position, while the mask (positioned upstream at a distance calculated during the design phase for generating the TG) is temporarily removed from the x-ray beam. As is customary in pump-probe experiments, the spatial and temporal overlap between x-rays and optical laser is achieved by measuring the beam position on a scintillator and observing changes in the laser's transmissivity after x-ray excitation. In our experiments, a bismuth germanate (BGO) sample has proven effective for this purpose [7]. Subsequently,

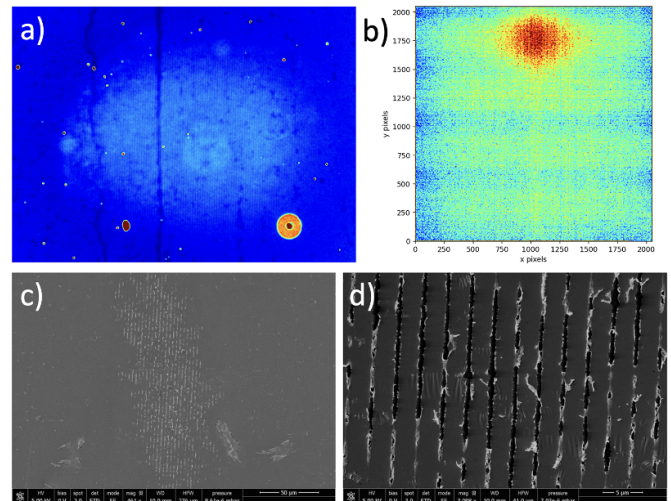


**Figure 4.** (a) The grating imprint is generated solely using x-rays with an energy density exceeding the damage threshold of the test sample. Once the imprints are created, the laser probe is employed exclusively to observe the static signal on the detector, as illustrated in (b). Subsequently, the phase-matching condition can be checked, and the positions of the D-mirror and detector adjusted accordingly. Panel (c) displays a scanning electron microscope (SEM) image of a permanent grating imprinted on a 10 nm film of gold. Notably, the irregular shape of the imprint indicates an irregular wavefront of the x-rays, in contrast to the elliptical-shaped imprint shown in (a). Panel (d) provides a zoomed-in view of panel (c).

the physical grating is introduced into the x-ray beam. In this initial phase, a forward diffraction signal from the transient grating can already be detected at the detector as a result of the pre-alignment process.

As mentioned in section 3.1, the period of the TG may slightly differ from that of the phase mask due to beam convergence/divergence, potentially causing the forward diffraction direction to be slightly misaligned or even missing. In such cases, several steps can be attempted, starting with an increase in both laser power and x-ray power below the sample damage threshold. If the signal remains elusive, we recommend elevating the x-ray power above the damage threshold to imprint a permanent grating (see figure 4(a)).

Subsequently, the x-rays can be blocked, and the laser can be diffracted by the permanent imprint on the test sample (see figure 4(b)). If imprinting the test sample proves unfeasible (possibly due to insufficient fluence), an alternative approach involves replacing the test sample with a gold-coated glass plate and irradiating it with a single x-ray shot at a moderate fluence. While this method facilitates easy printing, it necessitates a substantial reduction in laser power by orders of magnitude to prevent laser ablation and melting of the gold coating (see figures 4(c) and (d)). Once all parameters have been controlled, switching back to the test sample and performing the printing should yield the forward diffraction static signal (figure 4(b)). In both of the last two cases, the laser is diffracted by a permanent physical grating with the same period as the TG, and thus with the same geometry as for the time-resolved experiment. In this segment of the experiment, we recommend utilizing a camera to observe the permanent

signal. Permanent imprints are particularly valuable in this initial phase and whenever significant changes occur in the FEL machine parameters, as they offer direct insights into the quality of the transient grating and provide the exact pitch at the sample. The pitch of the grating can be measured using an optical microscope for micron-pitch sizes and a scanning electron microscope (SEM) or an atomic force microscope (AFM) for sub-hundred nanometre sizes.

Given that interference is employed to generate the TG on the sample, a high-quality wavefront of the x-ray beam is essential. Therefore, it is advisable to conduct a systematic investigation of the wavefront characteristics at the beginning of the beamtime. Although this process can be time-consuming, it is crucial for optimal performance. A Gaussian wavefront will yield a grating with a regular elliptical shape (see figure 4(a)), while a degraded wavefront may result in a less regular shape (see figure 4(c)). Importantly, an irregular TG shape would not necessarily compromise the quality of the data, as long as the XTG signal remains sufficiently intense.

#### 4. Detection and optimisation of the transient grating signal

Once the signal from the printed permanent grating has been identified, one can move to a new spot on the test sample. By reducing the x-ray fluence below the sample's damage threshold, selecting a temporal delay between laser and x-rays ( $\Delta t$ ) in the order of a few picoseconds (or a delay where the signal is expected to be strong), one should be able to observe the signal emanating from the transient grating. If the signal is absent or significantly weak, adjustments can be made to enhance its intensity. After exploring different temporal delays around the pump/probe overlap time ( $t_0$ ) and identifying the maximum, a scan along the direction of x-ray propagation (Z-scan) will reveal a sinusoidal trend characteristic of the Talbot carpet. In this process, it may become apparent that the weak signal was a result of the test sample being positioned in a minimum of the Talbot carpet, resulting in weak transient grating contrast and causing a less efficient excitation, as depicted in figure 5. Further optimization of the beam quality might be needed at this stage. The signal image at the CCD detector may appear irregular. Adjustments such as changing the laser spot size and fine-tuning the spatial overlap can help to achieve a regular shape. As a final step before commencing the actual experiment and measuring the sample of interest, preparation for the normalization of the x-rays is essential. If the beamline does not provide this parameter, it is typically collected using a piece of Kapton tape positioned in the x-ray path, and its scattering is measured by a photodiode, serving as the reference for  $I_{x\text{-rays}}$  on a shot-to-shot basis, similar to the laser's intensity. Figure 5(a) illustrates the overall setup.

At this stage, the XTG data is ready to be recorded on the test sample. The generation of the TG in the bulk of the sample initially results in an ultra-fast electronic response. The rapid rise of the signal is often modelled using an error function (erf),

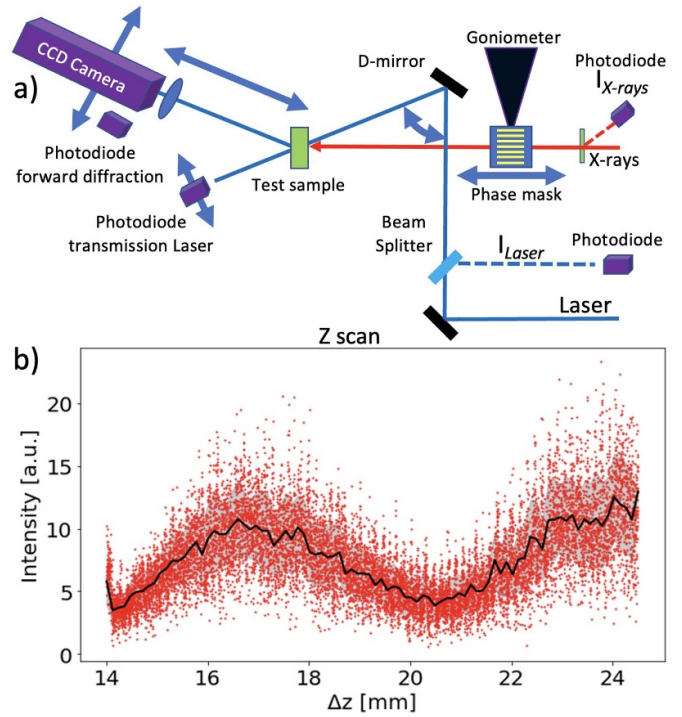


**Figure 5.** The complete schematic of the experiment, as employed at the FXE beamline of the EuXFEL, is presented in (a). Using the permanent grating some adjustments on the geometry can be implemented as suggested by the blue arrows. After that, the Z scan is conducted by setting  $\Delta t$  a few picoseconds after  $t_0$  and adjusting the position of the phase mask with respect to the sample within a range that is compatible with, or larger than, the anticipated period in the propagation direction, as shown in (b). In a preliminary approximation, the latter can be determined using equation (2). Once the Z scan is concluded,  $\Delta z$  should be set to the position of maximum to optimize the XTG signal.

accounting for the convolution between this fast response and the temporal resolution of the experiment. This is typically followed by a fast decay associated with electronic relaxation and a slower thermal decay. Additionally, sinusoidal oscillations due to excitation of phonons, magnons, charge density waves, etc are often observable. The overall typical fitting function, considering equation (3), can be expressed as:

$$I_{TG}(\Delta t) = \left| A \left[ \frac{1}{2} + \text{erf} \left( \frac{\Delta t}{\sigma} \right) \right] \times \left[ B e^{-\frac{\Delta t}{\tau}} - \sum_i C_i \cos(2\pi\nu_i \Delta t) e^{-\frac{\Delta t}{\tau_i}} \right] \right|^2 \quad (4)$$

providing the signal to be zero at  $\Delta t \leq 0$ . Here,  $\sigma$  is the width of the rising signal which matches the machine temporal resolution for fast samples as BGO,  $\tau$  is the thermal decay associated with the relaxation of the TG, and the oscillating terms represents oscillation with their given frequencies  $\nu_i$  and decay times  $\tau_i$ .

## 5. Increasing the repetition rate

The peculiarity of the EuXFEL lies in its ability to generate x-ray pulse trains at a repetition rate of 10 Hz, which can contain in between 1 and 2700 evenly separated x-ray pulses in a single train, corresponding to a maximum intra-train repetition rate of 4.5 MHz [15, 16]. During our experiment, the repetition rate was set to 141 kHz. This capability enables users to conduct measurements that once took weeks in a matter of hours if not minutes. However, to fully leverage the power of high repetition rates, an optical detection system capable of keeping pace with the x-ray's repetition rate is essential. Therefore, we combined classic CCD detection with photodiode detection, achieving single-shot acquisition of the x-ray Transient Grating (XTG) signal that can be obtained at the same repetition rate the same repetition rate of the x-ray pulses. This improvement enhances the statistics achievable in the same time window compared to CCD detection. This acquisition speed must also be obtained for the  $I_{\text{Laser}}$  and  $I_{\text{x-rays}}$  detection systems for normalization purposes. It is worth noting that the detection setup must ensure the linearity of the employed photodiodes and their (amplifier) power supplies.

In figure 6(a), we present the schematic of the collection of photodiode data using a train of 20 x-ray pulses (see figure 6(b)) and a train of 40 laser pulses, signifying that the TG on the sample is present every other laser pulse (see figure 6(c)). This is evident in the XTG signal in figure 6(b), where a high signal of 20 pulses (red dots) and a lower signal of 20 pulses, attributed to laser scattering, is observable (blue dots). These un-pumped shots, normalized by their respective  $I_{\text{Laser}}$  values, are used as a background subtraction factor. The x-ray train exhibits an intensity-decreasing pattern with the number of pulses, while conversely, the probe laser shows a slight increasing-intensity behaviour (indirectly visible in the XTG panel). This atypical behaviour (completely dependent on the sources i.e. the FEL machine and the laser, rather than on the detection system or eventual cumulative thermal response of the sample) serves as an ideal scenario to illustrate the fundamental importance of the normalization process, as shown in figure 10 through a comparison between the un-normalized traces (figure 10(a)) and their normalized counterparts (figure 10(b)).

## 6. Data analysis

The ability to conduct live data analysis is crucial as it provides valuable insights into the ongoing measurements, potentially influencing the experimental plan based on early results. Ensuring that the data analysis team can perform accurate analysis as soon as the first XTG scan is available is essential.

In exploring the dynamics of a sample, one of the critical parameters is the time arrival between the laser and x-ray pulses, which unfortunately is subject to jittering (up to a few tens of femtoseconds). If not corrected, this jitter can significantly impact the quality of the obtained data. Therefore, during data acquisition, it is extremely important to assess the arrival time jitter on a shot-to-shot basis. Different

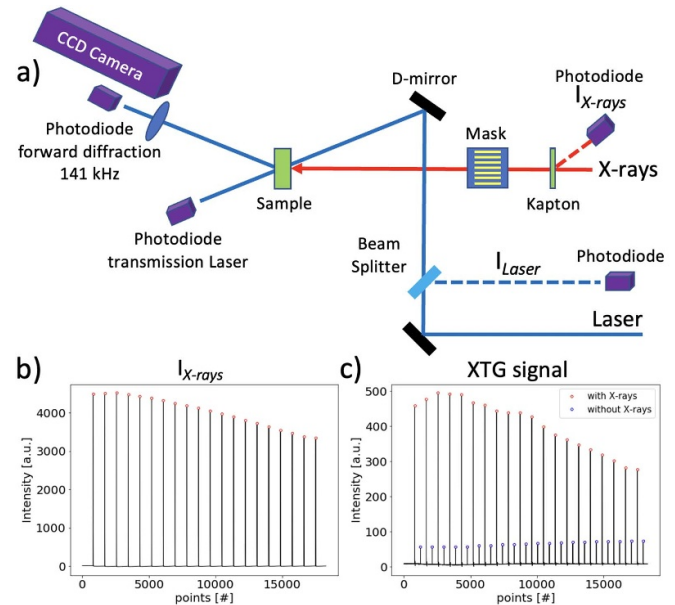


**Figure 6.** (a) illustrates the optimized experimental setup, where the detection of the XTG signal has been moved to the photodiode, which allows for a higher repetition rate acquisition compared to the camera. In (b), the photodiode signal is shown, observing a single train of x-ray pulses, i.e.  $I_{\text{x-rays}}$ , demonstrating the detection of a signal with 20 pulses. In (c), the trace of the photodiode capturing the XTG signal is presented. This trace contains 40 pulses, as the probe laser operates at 40 pulses for each x-ray train, i.e. the sample is pumped by the x-rays only every other laser shot. The photodiode output is higher when the x-rays are present (red dots) and lower when they are not (blue dots). These un-pumped shots are used for background subtraction purposes. The non-zero signal recorded by the photodiode (blue dots) is attributed to laser scattering in the experimental chamber. (b) depicts the x-rays decreasing in intensity with the number of pulses due to the FEL machine. (c) shows a slight increase in laser intensity (blue dots) with the number of pulses and a steep decrease in the XTG signal (red dots). The increase in the laser intensity is intrinsic to the laser and does not depend on the photodiode nor on an eventual cumulative thermal response of the sample since it has enough time to completely relax between subsequent shots. This decrease is due to the XTG signal being quadratically proportional to x-ray intensity and only linearly proportional to laser intensity.

facilities employ various approaches to employ this timing-tool correction, which must be implemented during data analysis. Nowadays, timing tools based on different methods are routinely used at XFELs, and their implementation in data analysis to correct for jitters and drifts is straightforward [17, 18].

Data from large-scale facilities contain numerous variables for every single shot and are typically stored in large h5 files. In the case of EuXFEL, a special Python library named 'extra\_data' is provided to enable the convenient importing of measurement data into Python scripts or notebooks as Xarray DataSets for further analysis. The treatment of the data varies depending on the detection system used to collect them.

### 6.1. Camera

In this specific case, every intensity except the XTG signal is recorded through a photodiode leading to shot-to-shot



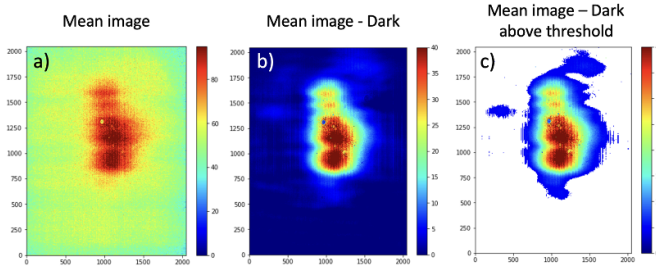


**Figure 7.** (a) displays the average image of the CCD trace. The signal, likely having an asymmetric shape due to the poor wavefront of the x-rays, is superimposed on a background. (b) illustrates the average image of the CCD after subtracting the dark, representing the average image of the CCD for the shots collected at  $\Delta t < 0$ . (c) presents the same image as (b), but considering only the points above a threshold to be defined based on the intensity of the signal. In this case, it is equal to the average value of the dark plus three times its standard deviation.

statistics, while the camera integrates intensity over each pulse train, thus acquiring images with 10 Hz. As a result, the XTG signal and the normalization factors need to be treated differently. In this subsection, we will focus on the treatment of the data from the CCD camera, while the photodiode’s signal will be described in the following section 6.2.

The camera used was a Basler (model acA2040-25gmNIR,  $2048 \times 2048$  pixels,  $5.5 \times 5.5 \mu\text{m}^2$ ), acquiring a single signal shot for each image recorded. When using a 2D-detector such as a CCD, it is crucial to ensure that the signal spot at the CCD is smaller than the field of view and, ideally, has enough background all around [19]. Figure 7(a) illustrates the raw average image of the XTG signal. As observed, the signal rises on top of a background which, when counted together with the actual signal, can distort the optimal reproduction of the dynamic. We have tested a few different strategies to account for the background. One method involves implementing a region of interest (ROI), i.e. a fixed portion of the CCD fully containing the signal and its possible jittering due to the ‘breathing’ and relaxation of the TG, and further considering another ROI far away from the signal as the background to subtract from the signal. However, this methodology can be time-consuming to implement, considering that the ROIs should be checked and adjusted trace-by-trace. Moreover, even far away from the maximum signal, the background may exhibit some signal features.

Another way to handle the background is by generating a background image from unpumped delays. When recording the delay-dependence of a sample, one typically scans delays both before and after the time overlap of the pump and probe pulses. Before time overlap i.e.  $\Delta t < 0$ , the detector should ideally have no signal, and everything collected can be considered background. We defined the dark as the average signal coming from the sample for the points having  $\Delta t < 0$ . Figure 7(b) illustrates the average of the CCD camera with the dark subtracted. Figure 7(c) illustrates our final approach. In this particular case, we consider the image with the dark subtracted, but we integrate only over the points above a threshold

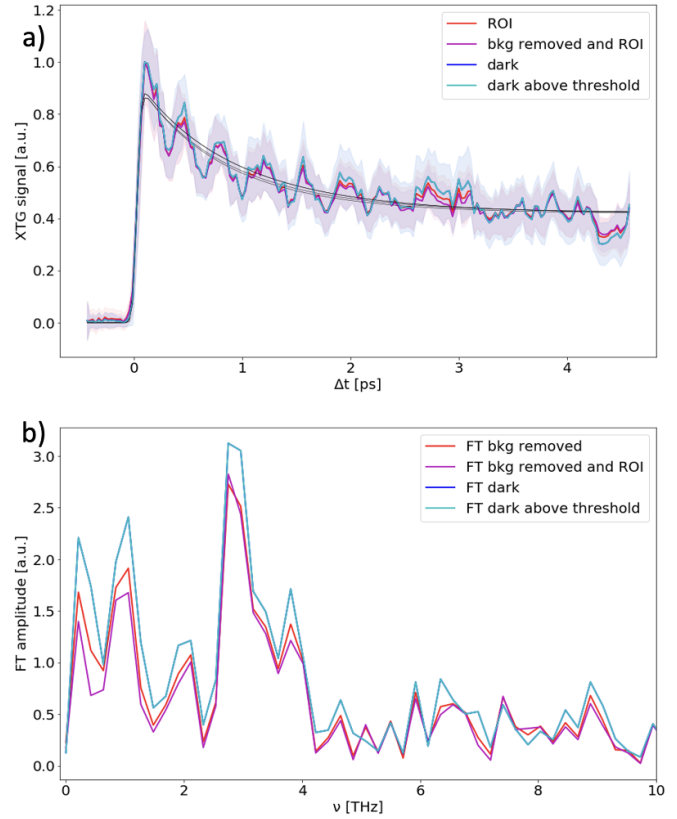


**Figure 8.** A comparison between different data analysis methodologies is presented. In (a), the red trace considers data points within an ROI surrounding the signal, while the magenta line considers points within the ROI and with background subtraction. The blue and cyan traces consider data points with dark subtraction only, and with dark subtraction and above a threshold, respectively. All traces were normalized following equation (3). Shades enveloping the traces correspond to their standard deviation. In (b), we show the respective Fourier Transforms (FT).

to be defined based on the intensity of the signal with respect to the background.

Figure 8 illustrates the dynamic of BGO in the first few picoseconds after excitation, detected using a CCD camera at 10 Hz and accumulating 50 shots per single delay, after normalization following equation (3). This trace provides the time resolution of the instrument with the rise-time ( $\sigma$ , in the order of  $\sim 100$  fs [20]), sufficient to observe modulations from excited optical phonons. An overlap with the error function (erf) multiplying a thermal decaying exponential is reported in black, leaving the isolated oscillation that is compatible with the optical phonon of BGO at 2.7 THz [7]. A comparison between the data analysis cases discussed above is also presented. A confrontation between red and magenta traces reveals a small change in considering or not considering the background subtraction to perform the integral of the image within an ROI. Considering or not considering a threshold barely changes the traces mainly due to the high-intensity signal and reduced background fluctuation compensated by the normalization procedure.

Using the dark image subtraction method, we remove from the data reduction process the need to manually set the ROIs,

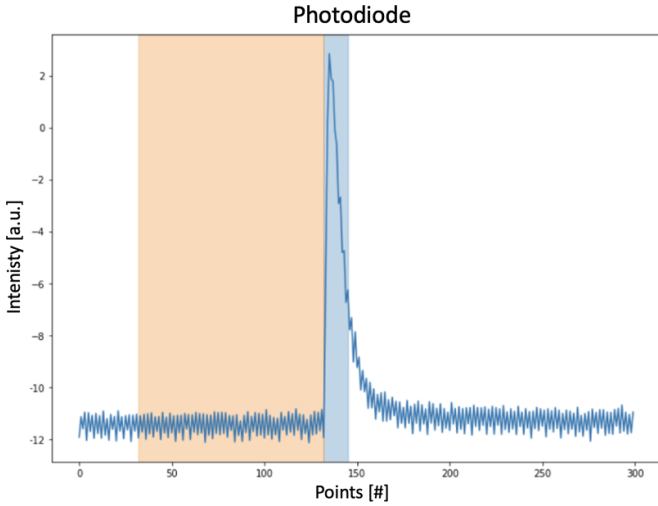


**Figure 9.** Signals detection with a photodiode. The background is selected as the mean of the 100 data points before the rise (orange box), and the signal is considered as the difference between the maximum of the rise (within the blue box) and the background. Not shown in figure, the background reaches its previous value before the subsequent rise.

saving a considerable amount of time during data analysis. As visible from the Fourier transforms (FTs) of the residuals (trace minus its exponential decay) in figure 8(b), the main feature at 2.7 THz in the Fourier space is slightly more enhanced considering the dark and a threshold than considering a simple ROI and the background. Even if the different methodologies lead to a similar result, the advantage of not setting ROIs manually leads to the conclusion that the ROI-less approach is the best method to use during the data analysis of a CCD camera for signals standing way above the background. However, this procedure has a drawback since it artificially reduces the noise of the image for  $\Delta t < 0$ . This artefact can be compensated by lowering the threshold at the expense of introducing more noise within the signal at  $\Delta t > 0$ . It is important to notice that this ROI-less approach above the threshold is particularly suited for high-intensity signals. When the signal is weak i.e. compatible with the background, the risk of subtracting part of the signal is high and must be managed with care.

### 6.2. Photodiode

Working at a high repetition rate with single-shot capabilities requires the use of photodiodes. Switching from CCD cameras to photodiodes is simple if the latter is mounted on the side of the CCD; a simple translation will place the photodiode in the right position to detect the signal. However, a dedicated lens in front of the diode is required since the chip size is usually much smaller than the CCD camera's. The photodiodes used were Thorlabs (model DET10A/M) while the digitizer was a Teledyne (model ADQ412, AC-coupled 4-channel up to 1.8 GS s<sup>-1</sup> sampling rate).

A zoom-in of a photodiode's trace is visible in figure 9. The background is selected as the mean of 100 data points before

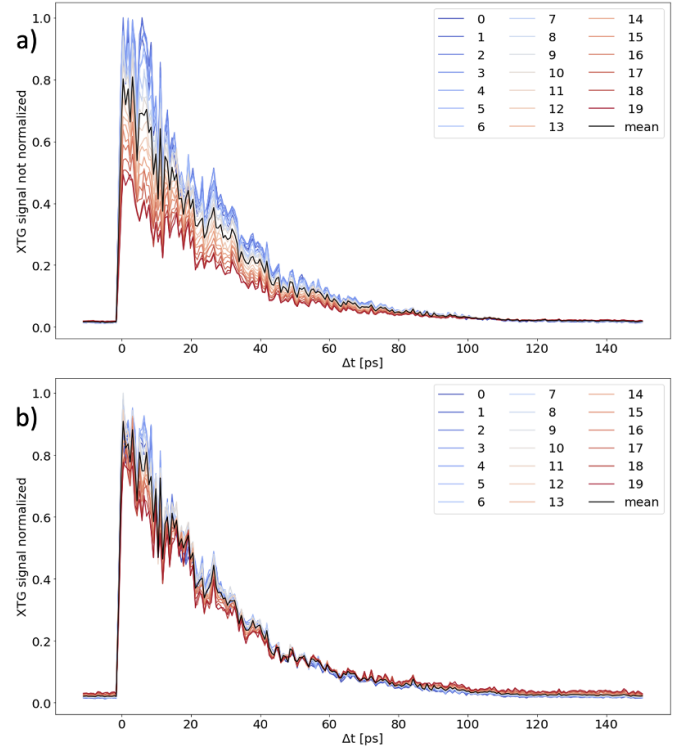


**Figure 10.** Illustrates the XTG signal detected with a photodiode. (a) presents the un-normalized traces obtained for each of the 20 x-ray pulses within the train, using a different colour for each order number, as indicated. (b) showcases the same traces normalized by  $I_{\text{Laser}}$  and  $I_{\text{x-rays}}$  according to equation (3). Different relaxation levels are reached by different order number traces due to the normalization procedure.

the rise (orange box). The value to be used for the signal can be set using the integral of the rise until the decay reaches the background level, or the integral until half maximum is reached during the signal decay, or as the maximum of the rise. Performing a comparison between these methodologies revealed an almost perfect correlation between them. Thus, it is suggested to use the easiest approach and collect the maxima for each spike, to be found within the blue box.

Figure 10(a) displays 20 un-normalized traces, acquired from a 20 nm thin film of polycrystalline Diamond sample. The XTG signal exhibits a declining pattern with the increasing order number of pulses, reflecting trends observed in both x-ray and Laser behaviours per pulse (refer to figure 6). This indicates the significance of acquiring shot-to-shot normalization factors  $I_{\text{x-rays}}$  and  $I_{\text{Laser}}$ . Upon application of these normalization factors, the resulting traces in figure 10(b) become suitable for statistical analysis.

## 7. Perspectives & conclusions

At this juncture, the preparation concludes, and the actual experiment can commence. Mount the real sample along with necessary equipment like a cryostat, magnet, liquid jet, etc bearing in mind the option of reflection detection if needed. Although this work focuses on a single detection channel,

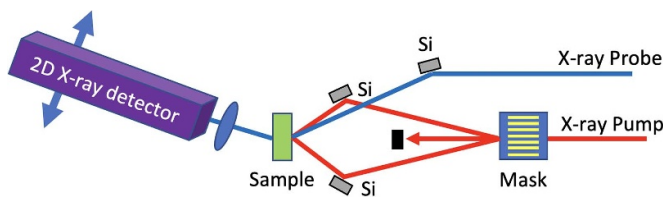


**Figure 11.** An illustration of the x-ray pump/x-ray probe Transient Grating. An x-ray pulse undergoes splitting via a phase mask (alternatively, if the mask cannot provide a sufficiently large angle to use Bragg mirrors, the usage of Laue crystal for splitting can be envisioned [24]) and is subsequently recombined on the sample using Bragg diffraction by silicon crystals. A third beam, the probe, also undergoes Bragg diffraction, arriving at the sample with the phase-matching condition angle. The resulting signal is then detected by the detection system.

polarization detection can be easily implementable by introducing a Wollaston prism before the detection point. This separates the signal into two polarization components, allowing the use of two identical detection devices instead of one, enabling polarization analysis, valuable for decoupling, such as distinguishing the thermo-elastic response from the magnetic one through the Magneto-optical Faraday effect (transmission detection) or the Magneto-optical Kerr effect (reflection detection) [21].

A beneficial enhancement to the setup could be heterodyne detection, involving the overlap of the signal with a local oscillator at the detector position. This enhances the signal-to-noise ratio and linearizes the signal concerning the incoming electric fields. However, implementing heterodyne detection [22, 23] introduces complexities in managing the optical laser, necessitating duplication through a split and recombination setup.

The Talbot effect offers a reliable and straightforward approach for x-ray TG pump/optical probe experiments. However, transitioning to an all-x-ray pump/probe scheme introduces some drawbacks. The primary limitation lies in the period achievable with physical gratings, typically in the order of tens of nanometres. This constrains attainable length scales and, consequently, the momentum transfer at the sample.

In our vision, realizing the full potential of the all-x-ray TG pump/probe necessitates a different approach illustrated in figure 11. Here, a single x-ray beam undergoes splitting using a mask and subsequent recombination through Bragg diffraction by silicon crystals, intersecting the x-ray beams on the sample. This configuration allows for smaller periodicities of the transient grating (down to fractions of an Angstrom), akin to the approach at TIMER—FERMI, allowing for the usage of an x-ray probe whose wavelengths can explore core edges. XFELs Beamlines already offer split and delay lines for multiple beams [25], yet they provide only a modest separation between the beams. Therefore, a dedicated optical system must be implemented to select the probe angle, ensuring it arrives at an appropriate angle to satisfy the phase-matching condition.

Finally, the exploration of core edges to perform spectroscopy can already be envisioned by adopting a self-diffraction approach where the measured signal arises from the diffraction

of the same x-rays responsible for generating the transient grating [4, 26]. This is not a time-resolved signal, however, it contains spectroscopic signatures whose intensity depends strongly on the sample's properties, similar to x-ray absorption spectroscopy. The main advantage of self-diffraction would be the detection of weak signals from thin layers (e.g. 2D material) or molecules, as well as the ability to access non-linear information of the sample such as third-order elements of the susceptibility, enabling the understanding of eventual influences on the signal given by the core level excitation.

This work is the result of the experimental campaigns at the Femtosecond x-ray Experiments (FXE) instrument at the EuXFEL. We have presented a reliable experimental setup and discussed in detail the experimental procedure (from the design to the alignment, from the optimisation of the signals to the data analysis) to perform x-ray transient grating/optical probe experiments at x-ray free electron lasers at low and high repetition rates.

### Data availability statement



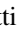


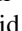


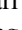
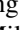


All data that support the findings of this study are included within the article (and any supplementary files). To be discussed upon reasonable request.

### Acknowledgments

The authors acknowledge the European XFEL facility for the Long Term Proposal 3323 granted to develop the x-ray transient grating technique. The physical gratings were manufactured by the Lab. for Micro and Nanotechnology group at Paul Scherrer Institute while the experiments were carried out at FXE instrument at EuXFEL. E P acknowledges funding from the European Union's Horizon 2020 research and innovation programme under the Marie Skłodowska-Curie Grant Agreement No. 860553. The work is partially supported under the Polish Ministry and Higher Education project: 'Support for research and development with the use of research infrastructure of the National Synchrotron Radiation Centre SOLARIS' under Contract No. 1/SOL/2021/2 and partially funded by the National Science Centre in Poland under Grant Number 2020/37/B/ST3/00555. M C acknowledges support via the ERC CHIRAX grant. R T acknowledges the MIUR Project: PRIN-2022JWAF7Y; EU Projects: I-PHOQS- IR0000016, ID-D2B8D520, CUP-B53C22001750006. The contribution by A A M, K A N, and N B was supported by the U.S. Department of Energy, Office of Science, Office of Basic Energy Sciences under Contract No. DE-SC0019126. R C, G R, M C e P C acknowledge support from Nanoscience Foundry and Fine Analysis (NFFA-MUR Italy Progetti Internazionali).

### ORCID iDs

Danny Fainozzi  <https://orcid.org/0000-0001-7380-8324>  
Filippo Bencivenga  <https://orcid.org/0000-0003-3929-5101>

Nadia Berndt  <https://orcid.org/0000-0001-9688-117X>  
 Martin Beye  <https://orcid.org/0000-0002-3924-2993>  
 Stefano Bonetti  <https://orcid.org/0000-0001-9352-2411>  
 Pietro Carrara  <https://orcid.org/0000-0002-1937-7591>  
 Majed Chergui  <https://orcid.org/0000-0002-4856-226X>  
 Christian David  <https://orcid.org/0000-0002-2953-1265>  
 Robin Y Engel  <https://orcid.org/0000-0002-2347-241X>  
 Eugenio Ferrari  <https://orcid.org/0000-0002-1082-5984>  
 Xinchao Huang  <https://orcid.org/0000-0002-9140-6369>  
 Christopher Milne  <https://orcid.org/0000-0003-4714-9139>  
 Carles Serrat  <https://orcid.org/0000-0002-9528-1938>  
 Renato Torre  <https://orcid.org/0000-0003-3182-9906>

## References

- [1] Chen G 2021 *Nat. Rev. Phys.* **3** 555
- [2] Johnson J A, Maznev A, Cuffe J, Eliason J K, Minnich A J, Kehoe T, Torres C M S, Chen G and Nelson K A 2013 *Phys. Rev. Lett.* **110** 025901
- [3] Foglia L et al 2023 *Photoacoustics* **29** 100453
- [4] Bencivenga F, Capotondi F, Foglia L, Mincigrucci R and Masciovecchio C 2023 *Adv. Phys.* **X 8** 2220363
- [5] Mincigrucci R et al 2018 *Nucl. Instrum. Methods Phys. Res. A* **907** 132
- [6] Svetina C et al 2019 *Opt. Lett.* **44** 574
- [7] Rouxel J R et al 2021 *Nat. Photon.* **15** 499
- [8] Weitkamp T, David C, Kottler C, Bunk O and Pfeiffer F 2006 *Proc. SPIE* **6318** 249–58
- [9] Kotov M M, Danko V P and Goloborodko A A 2021 *Opt. Lasers Eng.* **137** 106400
- [10] This is the general case of an amplitude grating. For a  $\pi/2$  phase grating  $m$  is replaced by  $m/2$ , while for a  $\pi$  phase grating  $m$  is replaced by  $m/8$ .
- [11] Teng S, Zhou T and Cheng C 2008 *Optik* **119** 695
- [12] Wen J, Zhang Y and Xiao M 2013 *Adv. Opt. Photonics* **5** 83
- [13] For nominal values of x-ray beam convergence, as per the simulation in figure 1(b), the TG periodicity decreases by  $0.2 \mu\text{m}$  (13.3%) over 150 mm in  $\Delta z$ . In this case, the Talbot plane's distance for every subsequent plane decreases by 0.25 mm.
- [14] Weitkamp T, Diaz A, Nohammer B, Pfeiffer F, Rohbeck T, Cloetens P, Stapanoni M and David C 2004 *Proc. SPIE* **5535** 137–42
- [15] Scholz M et al 2018 *Proc. 9th Int. Particle Accelerator Conf. (IPAC'18)* pp 29–33
- [16] Kujala N et al 2020 *Rev. Sci. Instrum.* **91** 103101
- [17] Divall M C, Romann A, Mutter P, Hunziker S and Hauri C P 2015 *Proc. SPIE* **9512** 303–12
- [18] Diez M et al 2023 *Nat. Commun.* **14** 2495
- [19] This condition is crucial to collect all the light of the signal and helps remove eventual background and signal fluctuations. These are indeed expected in SASE-based FELs e.g., the wave-front can fluctuate in shape due to machine parameters changing. A similar, but less revealing approach is used for the photodiode detection, where the background is estimated using the photodiode trace collected when there is no TG on the sample.
- [20] Khakhulin D et al 2020 *Appl. Sci.* **10** 995
- [21] Brioschi M, Carrara P, Polewczyk V, Dagur D, Vinai G, Parris P, Dal Zilio S, Panaccione G, Rossi G and Cucini R 2023 *Opt. Lett.* **48** 167
- [22] Torre R, Taschin A and Sampoli M 2001 *Phys. Rev. E* **64** 061504
- [23] Johnson J A, Maznev A A, Bulsara M T, Fitzgerald E A, Harman T, Calawa S, Vineis C, Turner G and Nelson K A 2012 *J. Appl. Phys.* **111** 023503
- [24] Bonse U and Hart M 1965 *Appl. Phys. Lett.* **6** 155
- [25] Alonso-Mori R et al 2015 *J. Synchrotron Radiat.* **22** 508
- [26] Morillo-Candas A et al 2023 *The European Conf. on Lasers and Electro-Optics* (Optica Publishing Group) p jsi\_1\_2